



# Optimisation of Trajectories for Wireless Power Transmission to a Quadrotor Aerial Robot

Murray L. Ireland<sup>1</sup>  · David Anderson<sup>1</sup>

Received: 15 November 2016 / Accepted: 26 March 2018  
© The Author(s) 2018

## Abstract

Unmanned aircraft such as multirotors are typically limited in endurance by the need to minimise weight, often sacrificing power plant mass and therefore output. Wireless power transmission is a method of delivering power to such aircraft from an off-vehicle transmitter, reducing weight whilst ensuring long-term endurance. However, transmission of high-powered lasers in operational scenarios carries significant risk. Station-keeping of the laser spot on the receiving surface is crucial to both ensuring the safety of the procedure and maximising efficiency. This paper explores the use of trajectory optimisation to maximise the station-keeping accuracy. A multi-agent model is presented, employing a quadrotor unmanned rotorcraft and energy transmission system, consisting of a two-axis gimbal, camera sensor and laser emitter. Trajectory is parametrised in terms of position and velocity at the extremes of the flight path. The optimisation operates on a cost function which considers target range, beam angle of incidence and laser spot location on the receiving surface. Several cases are presented for a range of variables in the trajectory and different conditions in the model and optimisation algorithm. Results demonstrate the viability of this approach in minimising station-keeping errors.

**Keywords** Trajectory optimisation · Quadrotor · Wireless power transmission · Simulated annealing · Nelder-Mead

## 1 Introduction

Wireless power transmission (WPT) is the transfer of electrical power without relying on standard contact media such as conductors or wires. Although the concept is not a new one [8], advancement of power transmitters and photosensitive receivers has made it more appealing in recent years. Whilst early investigations considered the use of microwave energy [7], several recent research programmes have favoured lasers [11, 18] especially for long-range transmission. WPT is particularly beneficial to systems which are limited in energy capacity, or which draw a large amount of power with respect to their total energy reserves.

An important contemporary example of such a system is the unmanned aerial vehicle (UAV). To remain airborne, an aircraft must generate enough lift to overcome its own weight. Weight minimisation is therefore a key consideration in the design of any aircraft and is especially so for rotorcraft, where the lifting force is produced exclusively by its rotors. Consider a rotorcraft with an all-electrical power system as typically favoured by UAVs, which draws power from an on-board cell array or battery. As the rotors are responsible for both balancing the weight and providing manoeuvring control of the vehicle, rotor power consumption is typically much higher than for fixed-wing aircraft of equivalent mass. Whilst it is possible to increase the energy available to the rotor or rotors by increasing the battery size or adding further cells, this only adds further weight and thus requires a greater lifting force. Further increasing the power consumption may then negate any potential benefits to flight time. This is particularly problematic in micro UAVs, or micro air vehicles (MAV), where the power supply contributes to a large fraction of the total vehicle mass.

Rather than attempt to compromise between the UAV's weight and endurance, consider an alternative. The UAV could carry only a minimal power supply, thus reducing its

---

✉ Murray L. Ireland  
Murray.Ireland@glasgow.ac.uk  
David Anderson  
Dave.Anderson@glasgow.ac.uk

<sup>1</sup> School of Engineering, James Watt (South) Building,  
University of Glasgow, Glasgow G12 8QQ, UK

weight. The flight time could then be extended indefinitely by supplying power remotely, using WPT. The operational benefits of such a hyper-extended endurance aircraft are numerous. Practical WPT could be implemented using either of two approaches. The first involves continuous WPT power supply, reducing the requirements of on-board power supply to emergency scenarios only. The second approach involves intermittent WPT supply, recharging a larger, but still limited, on-board battery at frequent intervals.

The feasibility of this approach has been demonstrated with application to both rotary- [1, 19] and fixed-wing [20] aircraft, all employing laser-based WPT. Some limitations in the demonstrated systems are evident. In the 12-hour quadrotor flight conducted by [1], the quadrotor's movement was restricted in the horizontal plane to a square of side 5 m. This was primarily to ensure that the laser remained on-target, thus minimising the risk of the laser striking another surface. Whilst such safeguards are necessary in early testing, restricting the movement of the quadrotor naturally limits its usefulness in many applications.

The primary concern with allowing unrestricted movement of the receiving system during WPT is the possibility of the laser missing its target and striking another surface, or missing the aircraft entirely. Given the power involved in such transmissions, this could be catastrophic. Additionally, poor station-keeping of the incident laser spot reduces the energy received by the system. These concepts are illustrated in Fig. 1. The laser can strike a surface other than the intended under two conditions. The first is that the beam diameter is greater than the projected dimensions of the receiving surface. Assuming the surface has been designed to be sufficiently large, this overfill has two potential causes: divergence of the beam over great distances; or a sufficiently large angle between the incident laser vector and the surface normal. The second condition is that the laser beam partially or entirely misses its target due to poor beam-steering. This

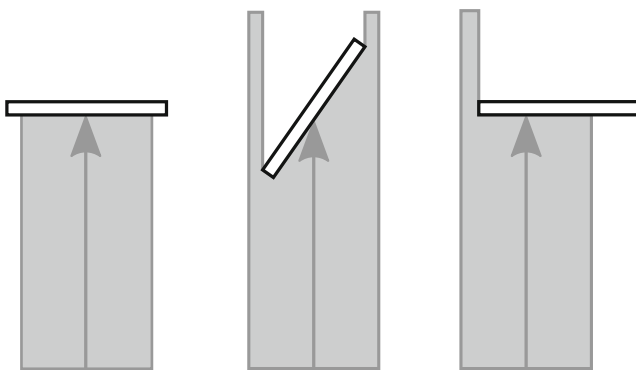


**Fig. 1** Visualisation of laser beam on-target (left), overfilling due to poor angle of incidence (centre) and partially missing due to poor beam-steering (right). (Note: laser beamwidth is enlarged for illustrative purposes)

may be caused by the receiving system manoeuvring too aggressively for the laser beam-steering system to keep up.

In allowing a UAV such as the quadrotor to freely perform its mission without heavy restrictions on movement, these hazards must be considered. One way to minimise the likelihood of tracking errors is to combine the quadrotor flight controller and laser beam-steering system tracking controllers into a single control system. However this architecture introduces additional complexity and robustness issues such as timely agent communication, lack of autonomy and swarm architecture inflexibility. Before proceeding apace with the design of such a complex, integrated control system it is worthwhile pausing to quantify the performance benefits obtainable from altering each controller's design aims, in particular optimising the UAV's flight trajectory such that the risk of beam overfilling or target miss are minimised or, ideally, eliminated.

This paper presents preliminary results of applying such an optimisation to the quadrotor guidance loop. The optimisation problem is presented as the minimisation of geometric errors in a multi-agent dynamic system. First, models of the agents in this system are discussed, including any relevant subsystems. Next, the optimisation problem is specified, including the errors to be minimised and the manipulated variables which enable this. A selection of results showing optimised trajectories are then presented and discussed. Finally, conclusions and future research directions are presented.

## 2 Modelling the Multi-agent Problem

The optimisation problem presented in this paper is specified as the minimisation of specific errors relating to the relative pose of two distinct agents. The first agent is the quadrotor aerial robot, which receives power via a photovoltaic array mounted on its frame. The second agent is an actuated energy transmission system (ETS), which consists of a laser emitter and electro-optical (EO) camera mounted on a two-axis gimbal, allowing accurate target tracking and sightline control. The gimbal is in the standard *elevation-over-azimuth* configuration affording the ETS's laser emitter and camera rotational freedom in elevation and heading [3, 4].

During ideal operation, the laser emitter projects a beam along a vector which is required to intersect with the geometric centre of the quadrotor's photovoltaic array. The EO camera is mechanically aligned to the laser emitter and provides feedback to the ETS's control system via "*see-spot*" tracking of the laser spot on the photovoltaic detector. It is thus necessary to consider the position and orientation of the photovoltaic sensor relative to both the laser emitter and EO camera. This requires accurate simulation of the geometry and dynamics of both systems.

### 2.1 Multi-agent Geometry

The geometry of the multi-agent system can be seen in Fig. 2. Both agents operate in an inertially-fixed World frame  $\mathcal{W}$ . For brevity, the reference frame  $\mathcal{W}$  is implied in the cases where a position vector  $\mathbf{r}$  or element lacks a superscript denoting an explicit frame of reference. The mechanics of the quadrotor are covered extensively in the literature and will not be described in depth here. For more detail, the reader is referred to [6, 12, 13, 21].

First consider the quadrotor. The quadrotor has six degrees of freedom: translational displacement  $\mathbf{r}_Q = [x_Q, y_Q, z_Q]^T \in \mathbb{R}^3$  and rotational displacement  $\boldsymbol{\eta} = [\phi, \theta, \psi]^T \in \mathbb{R}^3$ . A body-fixed frame  $\mathcal{Q}$  has origin at the quadrotor’s centre of mass. The orientation of  $\mathcal{Q}$  in  $\mathcal{W}$  is given by the direction cosine matrix

$$\mathbf{R}_Q^{\mathcal{W}} = \begin{bmatrix} c_\phi c_\psi & s_\phi s_\theta c_\psi - c_\phi s_\psi & c_\phi s_\theta c_\psi + s_\phi s_\psi \\ c_\phi s_\psi & s_\phi s_\theta s_\psi + c_\phi c_\psi & c_\phi s_\theta s_\psi - s_\phi c_\psi \\ -s_\theta & s_\phi c_\theta & c_\phi c_\theta \end{bmatrix} \quad (1)$$

where  $c_\phi$  denotes  $\cos \phi$ ,  $s_\theta$  denotes  $\sin \theta$  and so forth. This allows any position in  $\mathcal{Q}$  to be rotated to  $\mathcal{W}$  by  $\mathbf{r}^{\mathcal{W}} = \mathbf{R}_Q^{\mathcal{W}} \mathbf{r}^{\mathcal{Q}}$ . As  $\mathbf{R} \in SO(3)$ , the reverse transformation may be defined  $\mathbf{R}_{\mathcal{W}}^{\mathcal{Q}} = (\mathbf{R}_Q^{\mathcal{W}})^T$ .

The geometric centre of the quadrotor’s photovoltaic sensor has fixed position  $\mathbf{r}_{S/Q}^{\mathcal{Q}} \in \mathbb{R}^3$  in  $\mathcal{Q}$ , as shown Fig. 2. The

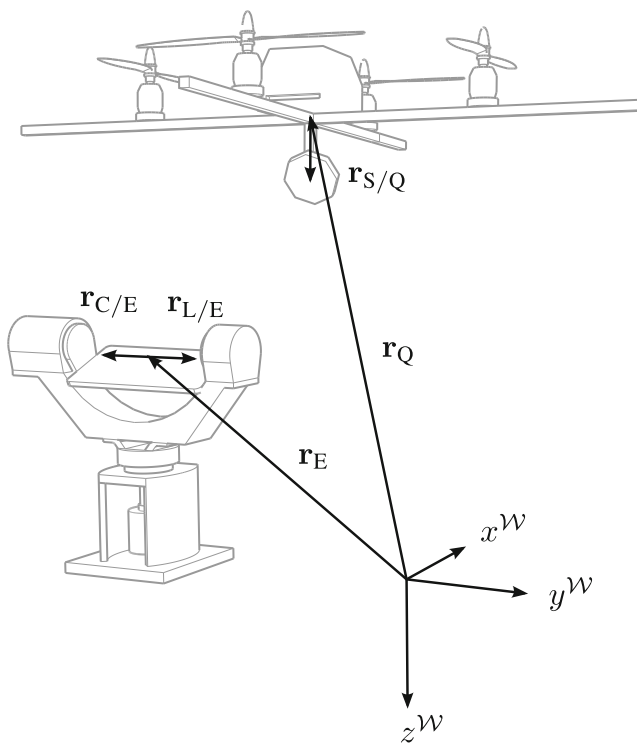


Fig. 2 Geometry of quadrotor and ETS agents, with associated subsystems, in inertial frame  $\mathcal{W}$

orientation of the sensor surface is defined by the surface normal  $\hat{\mathbf{n}}_S^{\mathcal{Q}} \in \mathbb{R}^3$ . The sensor thus has position and surface normal in  $\mathcal{W}$  defined by

$$\begin{aligned} \mathbf{r}_S &= \mathbf{r}_Q + \mathbf{R}_Q^{\mathcal{W}} \mathbf{r}_{S/Q}^{\mathcal{Q}} \\ \hat{\mathbf{n}}_S &= \mathbf{R}_Q^{\mathcal{W}} \hat{\mathbf{n}}_S^{\mathcal{Q}} \end{aligned}$$

The geometry of the ETS and its subsystems may be considered similarly. Consider Fig. 3. The ETS has two degrees of freedom: elevation  $\epsilon$  and azimuth  $\lambda$ . These states describe the rotational displacement of an actuated platform which is driven by two brushless motors (see [2] for details of the full equations of motion). The intersection of the elevation and azimuth axes has fixed position  $\mathbf{r}_E$  in  $\mathcal{W}$ . This position is taken as the origin of a reference frame  $\mathcal{E}$ , which is fixed on the actuated platform. The orientation of  $\mathcal{E}$  in  $\mathcal{W}$  is then given by the direction cosine matrix

$$\mathbf{R}_{\mathcal{E}}^{\mathcal{W}} = \begin{bmatrix} \cos \epsilon \cos \lambda & -\sin \lambda & \sin \epsilon \cos \lambda \\ \cos \epsilon \sin \lambda & \cos \lambda & \sin \epsilon \sin \lambda \\ -\sin \epsilon & 0 & \cos \epsilon \end{bmatrix} \quad (2)$$

with the reverse transformation  $\mathbf{R}_{\mathcal{W}}^{\mathcal{E}} = (\mathbf{R}_{\mathcal{E}}^{\mathcal{W}})^T$  applying.

The ETS’s EO camera and laser emitter are fixed on the actuated platform. The EO camera has fixed position  $\mathbf{r}_{C/E}^{\mathcal{E}} \in \mathbb{R}^3$  and line of sight unit direction vector  $\hat{\mathbf{n}}_C \in \mathbb{R}^3$  in

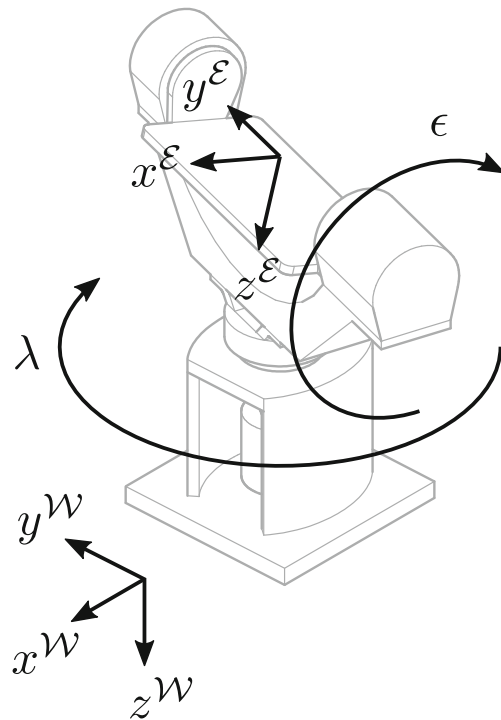


Fig. 3 Axes definition of reference frame  $\mathcal{E}$ , fixed on the ETS’s actuated platform

$\mathcal{E}$ . The camera position and line of sight are thus described in  $\mathcal{W}$  by

$$\begin{aligned} \mathbf{r}_C &= \mathbf{r}_E + \mathbf{R}_E^{\mathcal{W}} \mathbf{r}_{C/E}^{\mathcal{E}} \\ \hat{\mathbf{n}}_C &= \mathbf{R}_E^{\mathcal{W}} \hat{\mathbf{n}}_C^{\mathcal{E}} \end{aligned}$$

The laser similarly has source position  $\mathbf{r}_{L/E}^{\mathcal{E}} \in \mathbb{R}^3$  and unit direction vector  $\hat{\mathbf{n}}_L \in \mathbb{R}^3$  in  $\mathcal{E}$ . The position and direction vector in  $\mathcal{W}$  are thus

$$\begin{aligned} \mathbf{r}_L &= \mathbf{r}_E + \mathbf{R}_E^{\mathcal{W}} \mathbf{r}_{L/E}^{\mathcal{E}} \\ \hat{\mathbf{n}}_L &= \mathbf{R}_E^{\mathcal{W}} \hat{\mathbf{n}}_L^{\mathcal{E}} \end{aligned}$$

The geometry described here and shown in Fig. 2 may be used to define the errors for the optimisation problem. The agent geometry and thus the optimisation errors are subject to the dynamics and subsystem behaviours of the two agents, which may now be defined.

### 2.2 The Quadrotor

The quadrotor’s propulsion and control are provided by four rotors, each with input  $u_i, i = \{1, 2, 3, 4\}$ . The translational and rotational response of the quadrotor to inputs in  $u_i$  is described by a non-linear rigid body model. A non-linear dynamic inversion (NDI) controller with a linear state feedback provides a critically-damped response in closed loop [13].

#### 2.2.1 Vehicle Dynamics

The response of the quadrotor position  $\mathbf{r}_Q$  and attitude  $\boldsymbol{\eta}$  in  $\mathcal{W}$  to inputs in  $\mathbf{u} = [u_1, u_2, u_3, u_4]^T$  is described by

$$\begin{aligned} \ddot{\mathbf{r}}_Q &= g\hat{\mathbf{z}} - \frac{K_T}{m} \mathbf{R}_Q^{\mathcal{W}} \hat{\mathbf{z}} u_{\text{col}} \\ \ddot{\boldsymbol{\eta}} &= \mathbf{I}^{-1} \left( \begin{bmatrix} K_T L u_{\text{lat}} \\ K_T L u_{\text{long}} \\ K_Q u_{\text{yaw}} \end{bmatrix} - \dot{\boldsymbol{\eta}} \times \mathbf{I} \boldsymbol{\eta} \right) \end{aligned} \quad (3)$$

where  $m$  is the quadrotor mass,  $g$  is the acceleration due to gravity,  $K_T$  and  $K_Q$  are thrust and torque constants, respectively and  $\hat{\mathbf{z}}$  is the unit direction vector in the  $z$ -axis. The inertia tensor  $\mathbf{I}$  is the diagonal matrix

$$\mathbf{I} = \begin{bmatrix} I_x & 0 & 0 \\ 0 & I_y & 0 \\ 0 & 0 & I_z \end{bmatrix}$$

Equation 3 describes the elements of the pseudo-input vector

$$\mathbf{u}^* = [u_{\text{col}}, u_{\text{lat}}, u_{\text{long}}, u_{\text{yaw}}]^T$$

rather than the true inputs. This simplifies the definition of the model and control of the plant. The pseudo-inputs

are then related to the true inputs by the invertible matrix relationship

$$\mathbf{u}^* = \begin{bmatrix} 1 & 1 & 1 & 1 \\ 0 & 0 & 1 & -1 \\ -1 & 1 & 0 & 0 \\ -1 & -1 & 1 & 1 \end{bmatrix} \mathbf{u} \quad (4)$$

#### 2.2.2 Controller

An NDI controller is used to render the closed-loop dynamics of the quadrotor near-linear and simplify the gain-selection process. This ensures accurate tracking of specified trajectories. The four pseudo-inputs defined previously are specified by the control laws

$$\begin{aligned} u_{\text{col}} &= \frac{m [g - K_{z1}(z_d - z) - K_{z2}(\dot{z}_d - \dot{z})]}{K_T \cos \phi \cos \theta} \\ u_{\text{lat}} &= \frac{1}{K_T L} [I_x (K_{a1}(\phi_d - \phi) - K_{a2}\dot{\phi}) \\ &\quad + (I_z - I_y)\dot{\theta}\dot{\psi}] \\ u_{\text{long}} &= \frac{1}{K_T L} [I_y (K_{a1}(\theta_d - \theta) - K_{a2}\dot{\theta}) \\ &\quad + (I_x - I_z)\dot{\phi}\dot{\psi}] \\ u_{\text{yaw}} &= \frac{1}{K_Q} [I_y (K_{\psi1}(\psi_d - \psi) - K_{\psi2}\dot{\psi}) \\ &\quad + (I_y - I_x)\dot{\phi}\dot{\theta}] \end{aligned} \quad (5)$$

where  $\ddot{z}_d$  and  $\ddot{\boldsymbol{\eta}}_d$  are specified by the state feedback

$$\begin{aligned} \begin{bmatrix} \ddot{z}_d \\ \ddot{\boldsymbol{\eta}}_d \end{bmatrix} &= \begin{bmatrix} K_{z1} & 0 & 0 & 0 \\ 0 & K_{a1} & 0 & 0 \\ 0 & 0 & K_{a1} & 0 \\ 0 & 0 & 0 & K_{\psi1} \end{bmatrix} \begin{bmatrix} z_d - z \\ \boldsymbol{\eta}_d - \boldsymbol{\eta} \end{bmatrix} \\ &\quad + \begin{bmatrix} K_{z2} & 0 & 0 & 0 \\ 0 & K_{a2} & 0 & 0 \\ 0 & 0 & K_{a2} & 0 \\ 0 & 0 & 0 & K_{\psi2} \end{bmatrix} \begin{bmatrix} \dot{z}_d - \dot{z} \\ -\dot{\boldsymbol{\eta}} \end{bmatrix} \end{aligned} \quad (6)$$

which controls the three rotational degrees of freedom in  $\boldsymbol{\eta}$  and the height  $z$ . For clarity, the subscript Q has been omitted from the position elements in these equations. The true inputs  $\mathbf{u}$  are then obtained by inverting the relationship in Eq. 4.

To stabilise the zero dynamics,  $\phi_d$  and  $\theta_d$  must be defined such that a desired position in the horizontal plane  $x^{\mathcal{W}}-y^{\mathcal{W}}$  is reached. This is achieved by the non-linear feedbacks

$$\begin{aligned} \phi_d &= -\arcsin \left[ \frac{m(\ddot{x}_d \sin \psi - \ddot{y}_d \cos \psi)}{K_T u_{\text{col}}} \right] \\ \theta_d &= -\arcsin \left[ \frac{m(\ddot{x}_d \cos \psi + \ddot{y}_d \sin \psi)}{K_T u_{\text{col}} \cos \phi} \right] \end{aligned} \quad (7)$$

where  $\ddot{x}_d$  and  $\ddot{y}_d$  are specified by the state feedback

$$\begin{bmatrix} \ddot{x}_d \\ \ddot{y}_d \end{bmatrix} = K_{p1} \begin{bmatrix} x_d - x \\ y_d - y \end{bmatrix} + K_{p2} \begin{bmatrix} \dot{x}_d - \dot{x} \\ \dot{y}_d - \dot{y} \end{bmatrix} \quad (8)$$

The trajectory commands  $\mathbf{r}_{Q,d} = [x_d, y_d, z_d]^T$  and their derivatives are each specified by a polynomial function of time. The parameters of these polynomials are then the variables which are adjusted by the optimisation algorithm. This is described in more detail in the problem specification.

The heading command  $\psi_d$  is specified by a line-of-sight controller which points the horizontal component of the photovoltaic sensor's surface normal in the direction of the ETS. Assuming this surface normal is aligned such that  $\hat{\mathbf{y}}^Q \cdot \hat{\mathbf{n}}_S^Q = 0$ , the quadrotor's yaw command may be specified by

$$\psi_d = \arctan \frac{y_E - y_Q}{x_E - x_Q} \quad (9)$$

### 2.3 An Energy Transmission System

The ETS is modelled as a simple two degree-of-freedom system with first-order rotational dynamics. The inputs to the brushless motors may be considered the set-point commands for each degree of freedom, that is  $\mathbf{u}_E = [\epsilon_d, \lambda_d]^T$ . These commands are specified by a beam-steering controller which has multiple modes. Two of these modes rely on visual feedback from the EO camera.

#### 2.3.1 Platform Dynamics

The response in elevation and azimuth angles to the set-point commands is described by the first-order relationships

$$\begin{bmatrix} \dot{\epsilon} \\ \dot{\lambda} \end{bmatrix} = \frac{1}{\tau} \left( \mathbf{u}_E - \begin{bmatrix} \epsilon \\ \lambda \end{bmatrix} \right) \quad (10)$$

where  $\tau$  represents an abstraction of the electro-mechanical behaviour of the motors and the inertias of the ETS structure.

#### 2.3.2 EO Camera Model

The EO camera tracks the photosensitive sensor and the laser spot when it is incident on the sensor. The coordinates of the sensor and laser spot in the camera image are then provided to the ETS controller. A suitable camera model is thus required (Fig. 4).

The position of a point P, fixed in the quadrotor body frame  $Q$  may be described in the ETS platform-fixed frame  $\mathcal{E}$  by transforming it first to  $\mathcal{W}$  and then  $\mathcal{E}$ . The position of P  $\mathbf{r}_P$  is thus described relative to the camera position  $\mathbf{r}_C$  in  $\mathcal{E}$  by

$$\mathbf{r}_{P/C}^{\mathcal{E}} = \mathbf{R}_{\mathcal{W}}^{\mathcal{E}} \left( \mathbf{r}_Q - \mathbf{r}_E + \mathbf{R}_Q^{\mathcal{W}} \mathbf{r}_{P/Q}^Q \right) - \mathbf{r}_{C/E}^{\mathcal{E}} \quad (11)$$

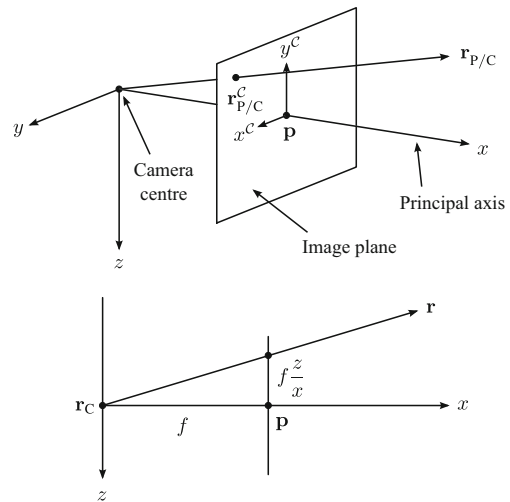


**Fig. 4** Geometry of a generic pinhole camera model. The camera centre C is at the centre of the coordinate system, with position  $\mathbf{r}_C$  in Euclidean 3-space. A point P has position  $\mathbf{r}_{P/C}$  relative to C in 3-space. This point may be mapped to 2-space by considering the intersection of the relative position vector with the image plane. The image plane is normal to the principal axis  $x$  and is fixed at point  $\mathbf{p}$  along this axis

If  $\mathbf{r}_{P/C}^{\mathcal{E}} = [x_{P/C}^{\mathcal{E}}, y_{P/C}^{\mathcal{E}}, z_{P/C}^{\mathcal{E}}]^T$  describes the position of P in *object space*, the position in *camera space* is described by

$$\mathbf{x}_P^C = f \frac{y_{P/C}^{\mathcal{E}}}{x_{P/C}^{\mathcal{E}}} \quad \mathbf{y}_P^C = -f \frac{z_{P/C}^{\mathcal{E}}}{x_{P/C}^{\mathcal{E}}} \quad (12)$$

The camera has field of view  $\varphi$  and aspect ratio  $A$ . For P to be visible to the camera, it must therefore satisfy the constraints

$$\begin{aligned} -f \tan \varphi &\leq x_P^C \leq f \tan \varphi \\ -\frac{f}{A} \tan \varphi &\leq y_P^C \leq \frac{f}{A} \tan \varphi \end{aligned}$$

#### 2.3.3 Laser Model

The laser beam is modelled as a beam of finite length, originating at the point  $\mathbf{r}_L$ , which is fixed in  $\mathcal{E}$ . The beam terminates at the laser spot position  $\mathbf{r}_{LS}$ , where it intersects the surface plane of the photovoltaic sensor on the quadrotor. The laser spot position may be given by

$$\mathbf{r}_{LS} = l \hat{\mathbf{n}}_L + \mathbf{r}_L \quad (13)$$

where  $l$  is the beam length from source to terminal.

The laser spot only exists if it intersects this plane within the area defined by the sensor surface. Otherwise, the beam length is assumed to be infinite. Assuming a circular sensor surface of radius  $r_S$  and centre  $\mathbf{r}_S$ , the beam length is thus defined by

$$l = \begin{cases} \frac{(\mathbf{r}_S - \mathbf{r}_L) \cdot \hat{\mathbf{n}}_S}{\hat{\mathbf{n}}_L \cdot \hat{\mathbf{n}}_S} & \text{if } \|\mathbf{p} - \mathbf{r}_S\| \leq r_S \\ \infty & \text{if } \|\mathbf{p} - \mathbf{r}_S\| > r_S \end{cases} \quad (14)$$

where  $\mathbf{p}$  is the point of intersection of the laser vector and the infinite surface plane of the sensor.

### 2.3.4 Beam-Steering Controller

The purpose of the ETS controller is to ensure that the laser spot remains incident on the photovoltaic sensor and close to its centre at all times. Whilst no “off” state for the laser beam is included in the model, it is assumed that the laser is not activated until there is confidence that it will be immediately incident on the surface. To achieve this, it has three modes.

First, *seek* mode directs the principal axis of the EO camera towards the quadrotor position  $\mathbf{r}_Q$ , which is known and communicated to the ETS. This is achieved using the simple sightline controller

$$\begin{aligned} \tan \lambda_d &= -\frac{z_Q - z_E}{\sqrt{(x_Q - x_E)^2 + (y_Q - y_E)^2}} \\ \tan \epsilon_d &= \frac{y_Q - y_E}{x_Q - x_E} \end{aligned} \tag{15}$$

The quadrotor is assumed to be at sufficient distance and the camera assumed to have sufficient field of view that this operation will result in the camera visually acquiring the quadrotor.

The controller then enters *sensor tracking* mode. The sensor is modelled as having a ring of LEDs around its circumference, which are now visible to the EO camera. The centroid of the  $N$  LEDs then corresponds to the sensor position  $\mathbf{r}_S$  and is found in camera space  $\mathcal{C}$  from

$$\mathbf{r}_S^C = \frac{1}{N} \sum_{i=1}^N \mathbf{r}_i^C$$

where  $\mathbf{r}_i$  describes the position of some LED  $i$ .

A proportional-integral (PI) controller then drives the system to centre  $\mathbf{r}_S^C$  within the camera frame, with the control law

$$\mathbf{u}_E = \tau \left( K_p \mathbf{e} + K_i \int \mathbf{e} dt \right) + \begin{bmatrix} \epsilon \\ \lambda \end{bmatrix} \tag{16}$$

where the error  $\mathbf{e} \in \mathbb{R}^2$  is simply the coordinates of the centroid in camera space  $\mathbf{e} = \mathbf{r}_S^C$ .

When the LED centroid is centred in  $\mathcal{C}$  within some tolerance, the controller enters *laser spot tracking* mode. The controller acts to centre the laser spot, now incident on the sensor surface, at the sensor position  $\mathbf{r}_S$ . The controller described by Eq. 16 is again used, whilst the error is now specified by

$$\mathbf{e} = \mathbf{r}_S^C - \mathbf{r}_{LS}^C \tag{17}$$

## 3 The Optimisation Problem

The optimisation problem is presented as the minimisation of three geometric errors by way of 18 possible variables. These variables describe the commanded trajectory of the quadrotor. The errors describe the relative geometries of the two agents, and are thus subject to the dynamics and subsystems of these agents.

### 3.1 Optimisation Variables: Describing the Trajectory

The desired trajectory  $\mathbf{r}_{Q,d} = [x_d, y_d, z_d]^T$  of the quadrotor is specified in each degree of freedom by a fifth-order polynomial [5, 10]. The desired trajectory in  $x$  is thus expressed by

$$\begin{aligned} x_d(t) &= a_0 + a_1 t + \frac{1}{2} a_2 t^2 + \frac{1}{6} a_3 t^3 \\ &\quad + \frac{1}{12} a_4 t^4 + \frac{1}{20} a_5 t^5 \end{aligned} \tag{18}$$

Differentiating this expression provides the desired trajectory of  $\dot{x}$

$$\dot{x}_d(t) = a_1 + a_2 t + \frac{1}{2} a_3 t^2 + \frac{1}{3} a_4 t^3 + \frac{1}{4} a_5 t^4 \tag{19}$$

whilst the desired trajectory of  $\ddot{x}$  may be found similarly

$$\ddot{x}_d(t) = a_2 + a_3 t + a_4 t^2 + a_5 t^3 \tag{20}$$

The time at the beginning of the trajectory may be denoted  $t_0$  and the time at the end  $t_f$ . Then if  $x_d(t_0) = x_0$ ,  $\dot{x}_d(t_f) = \dot{x}_f$  and so forth, it is possible to relate the desired position, velocity and acceleration at each end of the trajectory to the coefficients  $a_i$ ,  $i = \{1, 2, 3, 4, 5\}$  by the matrix relationship

$$\begin{bmatrix} x_0 \\ \dot{x}_0 \\ \ddot{x}_0 \\ x_f \\ \dot{x}_f \\ \ddot{x}_f \end{bmatrix} = \begin{bmatrix} 1 & t_0 & \frac{1}{2} t_0^2 & \frac{1}{6} t_0^3 & \frac{1}{12} t_0^4 & \frac{1}{20} t_0^5 \\ 0 & 1 & t_0 & \frac{1}{2} t_0^2 & \frac{1}{3} t_0^3 & \frac{1}{4} t_0^4 \\ 0 & 0 & 1 & t_0 & t_0^2 & t_0^3 \\ 1 & t_f & \frac{1}{2} t_f^2 & \frac{1}{6} t_f^3 & \frac{1}{12} t_f^4 & \frac{1}{20} t_f^5 \\ 0 & 1 & t_f & \frac{1}{2} t_f^2 & \frac{1}{3} t_f^3 & \frac{1}{4} t_f^4 \\ 0 & 0 & 1 & t_f & t_f^2 & t_f^3 \end{bmatrix} \begin{bmatrix} a_0 \\ a_1 \\ a_2 \\ a_3 \\ a_4 \\ a_5 \end{bmatrix} \tag{21}$$

For any desired  $x_0$ ,  $x_f$  and their derivatives, the coefficients of the smooth polynomials  $x_d(t)$  and  $\dot{x}_d(t)$  may be found by solving Eq. 21 for  $a_0, a_1, \dots, a_5$ . The desired trajectories in  $y$  and  $z$  are constructed similarly. Thus, the desired trajectory in each degree of freedom may be determined by specifying initial and final conditions for time, position, velocity and acceleration. The trajectory commands for position and velocity at any time  $t$  are then supplied to the quadrotor controller, as described by Eqs. 5 to 8.

In this instance, it is assumed that  $t_0 = 0$ , whilst  $t_f$  is fixed for a given manoeuvre. This leaves the 18 possible variables,  $\{\mathbf{r}_0, \dot{\mathbf{r}}_0, \ddot{\mathbf{r}}_0, \mathbf{r}_f, \dot{\mathbf{r}}_f, \ddot{\mathbf{r}}_f\} \in \mathbb{R}^3$ . The complete set of possible variables is defined as

$$\hat{\chi} = [\mathbf{r}_0^T, \dot{\mathbf{r}}_0^T, \ddot{\mathbf{r}}_0^T, \mathbf{r}_f^T, \dot{\mathbf{r}}_f^T, \ddot{\mathbf{r}}_f^T]^T \in \mathbb{R}^{18} \tag{22}$$

Rather than optimise the trajectory for all variables  $\hat{\chi}$ , a subset  $\chi \subseteq \hat{\chi}$  is defined. The remaining variables in  $\hat{\chi}$  are fixed constant. This allows the viability of this trajectory generation method to be considered on a smaller scale.

### 3.2 Errors

The cost function employed in the optimisation describes three scalar errors, each related to the geometry of the quadrotor-ETS system. Each error  $e_i, i = \{1, 2, 3\}$  is weighted by a scalar  $Q_i$  or matrix  $\mathbf{Q}_i$  and normalised with respect to a nominal maximum  $M_i$ .

Recall the description of the laser interaction with the photovoltaic sensor, illustrated in Fig. 1. To minimise the possibility of overflowing or partially missing the sensor, the projected area of the sensor in the direction of the laser vector must be maximised. This is achieved by considering the angle of incidence  $\gamma$  between the sensor normal and the laser vector, given by

$$\cos \gamma = -\hat{\mathbf{n}}_S \cdot \hat{\mathbf{n}}_L \tag{23}$$

The yaw autopilot described by Eq. 9 acts to minimise  $\gamma$  in the horizontal plane. The quadrotor trajectory is then optimised to aid the yaw autopilot and produce an attitude which minimises the angle in the vertical plane. Thus, to minimise the expression  $(\cos \gamma_d - \cos \gamma)$ , where  $\gamma_d = 0$ , the error function  $e_1$  is defined

$$e_1 = \frac{Q_1}{M_1^2} \left(1 + \hat{\mathbf{n}}_S^T \hat{\mathbf{n}}_L\right)^2 \tag{24}$$

where  $M_1 = 1$  and  $Q_1 = 1$ .

The trajectory pursued by the quadrotor also impacts the beam-steering accuracy of the ETS. To avoid defining a trajectory which is too aggressive for accurate beam-steering, the error between the centroid of the photovoltaic sensor  $\mathbf{r}_S$  and the laser spot position on the sensor  $\mathbf{r}_{LS}$  is minimised by

$$e_2 = \frac{1}{M_2^2} (\mathbf{r}_{LS} - \mathbf{r}_S)^T \mathbf{Q}_2 (\mathbf{r}_{LS} - \mathbf{r}_S) \tag{25}$$

where  $M_2 = 0.05$  and

$$\mathbf{Q}_2 = \begin{bmatrix} 1 & 0 & 0 \\ 0 & 1 & 0 \\ 0 & 0 & 1 \end{bmatrix}$$

Finally, the the distance between the laser emitter and the receiving sensor is minimised. This minimises beam divergence and reduces the energy loss due to atmospheric attenuation. The error is simply

$$e_3 = \frac{1}{M_3^2} (\mathbf{r}_S - \mathbf{r}_L)^T \mathbf{Q}_3 (\mathbf{r}_S - \mathbf{r}_L) \tag{26}$$

where  $M_3 = 50$  and

$$\mathbf{Q}_3 = \begin{bmatrix} 0.001 & 0 & 0 \\ 0 & 0.001 & 0 \\ 0 & 0 & 0.001 \end{bmatrix}$$

### 3.3 Cost Function

The optimisation problem is then formulated as a cost function  $\Phi(\chi)$  which is subject to the dynamics, controllers and trajectories of both agents. The problem is thus specified by

$$\begin{aligned} & \min_{\chi \subseteq \hat{\chi} \in \mathbb{R}^{18}} \Phi(\chi) \quad \text{for } t \in [t_0, t_f] \\ & \text{subject to } \dot{\mathbf{x}}_Q(t) = f_Q(\mathbf{x}_Q(t), \mathbf{r}_{Q,d}(t), \psi_d(t)) \\ & \quad \dot{\mathbf{x}}_E(t) = f_E(\mathbf{x}_E(t), \mathbf{u}_E(t)) \\ & \quad \mathbf{r}_{Q,d}(t) = g_{QR}(\hat{\chi}, t_0, t_f) \\ & \quad \psi_{Q,d}(t) = g_{Q\psi}(\mathbf{x}_Q(t), \mathbf{x}_E(t)) \\ & \quad \mathbf{u}_E(t) = g_E(\mathbf{x}_Q(t), \mathbf{x}_E(t)) \end{aligned} \tag{27}$$

where  $f_Q$  describes the closed-loop quadrotor dynamics and controller,  $f_E$  describes the closed-loop ETS response,  $g_{QR}$  and  $g_{Q\psi}$  respectively describe the trajectory and heading commands of the quadrotor and  $g_E$  describes the ETS pan and tilt commands.

The cost function  $\Phi(\chi)$  is then specified as

$$\Phi(\chi) = \int_{t_0}^{t_f} [e_1(t) + e_2(t) + e_3(t)] dt \tag{28}$$

where the errors  $\{e_1, e_2, e_3\} \geq 0 \in \mathbb{R}$  are dependent on the relevant geometry of the multi-agent system.

### 3.4 Algorithm

The trajectory is optimised by the non-linear Nelder-Mead method first proposed by [17] and adapted by [15]. This approach employs a simple line-search algorithm to accurately identify local minima. In one of the cases presented, simulated annealing is employed to approximately determine the global minima within a specific search space. This method was independently developed by [14] and [9]. Both algorithms were inspired by a mathematical model of the physical process of annealing, which was developed by [16].

## 4 Results

The optimisation is performed in MATLAB and considers a specific scenario. A quadrotor with a photovoltaic sensor enters a volume of space, at which time the ETS visually acquires the sensor and emits the laser onto its surface. The quadrotor then follows a curved flight path which is defined by the variables described in Eq. 22. The quadrotor follows this flight path for a short period of time before leaving the ETS's volume of interest. This scenario is designed to provide a specific test case and does not necessarily reflect the reality of a WPT operation. Methods of increasing the realism of the simulation are discussed at the end of the paper.

Whilst there are 18 possible variables which can be selected by the optimisation, there is no particular requirement to vary all 18. Instead, subsets of  $\hat{\chi}$  are optimised, whilst the remaining "variables" are held constant. Three such subsets are considered. The first subset describes only two variables, the second considers four and the third considers six. For each subset, two different cases are considered.

### 4.1 Simulation Setup

The quadrotor is commanded to follow a trajectory  $\mathbf{r}_{Q,d}(t)$ , beginning at  $t_0 = 0$  and finishing at  $t_f$ . The ETS is positioned at the origin of the  $x$ - $y$  plane in  $\mathcal{W}$ . The quadrotor starts with some position  $\mathbf{r}_0 = [0, y_0, z_0]^T$  and has final destination  $\mathbf{r}_f = [0, y_f, z_f]^T$ . The accelerations commands  $\ddot{\mathbf{r}}_0$  and  $\ddot{\mathbf{r}}_f$  are fixed at zero in each case. The initial and final velocities,  $\dot{\mathbf{r}}_0$  and  $\dot{\mathbf{r}}_f$  respectively, then define the flight trajectory.

The simulation is initialised such that the laser vector  $\hat{\mathbf{n}}_L$  is in the direction of the sensor position  $\mathbf{r}_S$ . This is done to reduce large values in the optimisation errors which would swamp smaller errors and reduce the effectiveness of the optimisation. The quadrotor is similarly yawed such that the sensor normal  $\hat{\mathbf{n}}_S$  is in the direction of the ETS position  $\mathbf{r}_E$ .

The simulation models use properties taken from system identification of the Qball-X4 quadrotor, supplied by Quanser,<sup>1</sup> and a bespoke ETS system. These properties are provided in Table 1, at the end of the paper.

### 4.2 Optimisation with Two Variables

The trajectory is parameterised by two variables  $\chi = \{\dot{x}_0, \dot{x}_f\}$ , whilst the remainder of the parameter set  $\hat{\chi} \setminus \chi$  is constant. The optimisation is performed for two cases. The first is a 10 s flight at short range, whilst the second is a 20 s flight at longer range. For each case, the quadrotor tra-

jectory is optimised for WPT using the two aforementioned variables only.

#### 4.2.1 Case 1: 10 s

The quadrotor trajectory is defined by the initial position  $\mathbf{r}_0 = [0, 10, -2]^T$  at  $t_0 = 0$  s and final position  $\mathbf{r}_f = [0, -10, -2]^T$  at  $t_f = 10$  s. The constant velocity parameters are fixed at  $\{\dot{y}_0, \dot{z}_0, \dot{y}_f, \dot{z}_f\} = 0$ . The trajectory is optimised for the two-parameter set  $\chi = \{\dot{x}_0, \dot{x}_f\}$  over the time range  $[t_0, t_f]$ , with initial values  $\chi_0 = \{5, -5\}$ .

Employing the Nelder-Mead line-search algorithm, a local minima is identified at the coordinates given in Table 3. The resulting trajectory is shown in Fig. 5. Asymmetry in the trajectory about the  $x$ -axis is immediately evident. The constituent errors and cumulative cost function during a flight with the optimised trajectory parameters can be seen in Fig. 6. Here, it can be seen that the error relating to beam angle of incidence,  $e_1$ , is largest at the end of the trajectory. Conversely, the error relating to the laser spot position on the sensor,  $e_2$ , dominates at the beginning of the trajectory. This is caused by initial beam-steering errors in the ETS's visual tracking system as the quadrotor enters its field of perception. Thus, the large difference in velocity for the initial and final trajectory properties is clearly due to the optimisation algorithm pursuing two goals. First, to reduce  $e_1$  at the end of the trajectory, it increases the desired velocity at this location  $\dot{x}_f$ . This adjusts the shape of the trajectory such that the vehicle attitude during the final second minimises  $e_1$ . The second goal, reducing the large spot position error  $e_2$ , requires that the initial velocity command  $\dot{x}_0$  is reduced. This improves the ETS's ability to visually capture the photovoltaic sensor and centre the laser spot upon it. The resulting minimised cost function at the end of the flight is  $\Phi_{\min} = 0.455$ .

For the two-variable optimisation, Eq. 27 may be considered a non-linear function of two properties,  $\dot{x}_0$  and  $\dot{x}_f$ , with a single output  $\Phi$ . This may be represented graphically as a two-dimensional contour map with elevation  $\Phi$ , as shown in Fig. 7. The contour map confirms that a local minima has been identified by the optimisation algorithm. Owing to the complexity of the non-linear function in this instance, it cannot be stated with any certainty that a global minima has been found.

#### 4.2.2 Case 2: 20 s

The quadrotor trajectory is defined by the initial position  $\mathbf{r}_0 = [0, 20, -3]^T$  at  $t_0 = 0$  s and final position  $\mathbf{r}_f = [0, -20, -3]^T$  at  $t_f = 20$  s. The constant velocity parameters are fixed at  $\{\dot{y}_0, \dot{z}_0, \dot{y}_f, \dot{z}_f\} = 0$ . The trajectory is optimised

<sup>1</sup>Quanser Consulting, Inc <http://www.quanser.com>

**Table 1** Simulation model properties

Property	Symbol	Value	Unit
EO camera aspect ratio	$A$	0.75	–
EO camera focal length	$f$	601.8	pixel
Moment of inertia about $x^{\mathcal{Q}}$	$I_x$	0.032	kg m <sup>2</sup>
Moment of inertia about $y^{\mathcal{Q}}$	$I_y$	0.033	kg m <sup>2</sup>
Moment of inertia about $z^{\mathcal{Q}}$	$I_z$	0.041	kg m <sup>2</sup>
Quadrotor attitude controller gain	$K_{a1}$	380.25	–
Quadrotor attitude controller gain	$K_{a2}$	39	–
ETS controller integral gain	$K_i$	2.5274	–
ETS controller proportional gain	$K_p$	0.1296	–
Quadrotor position controller gain	$K_{p1}$	3.8025	–
Quadrotor position controller gain	$K_{p2}$	3.9	–
Quadrotor height controller gain	$K_{z1}$	3.8025	–
Quadrotor height controller gain	$K_{z2}$	3.9	–
Quadrotor yaw controller gain	$K_{\psi1}$	0.6084	–
Quadrotor yaw controller gain	$K_{\psi2}$	1.56	–
Torque gain	$K_Q$	1.919	N m
Thrust gain	$K_T$	119.6	N
Moment arm of rotors	$L$	0.2	m
Quadrotor mass	$m$	1.512	kg
Number of sensor diodes	$N$	8	–
Direction vector of camera in $\mathcal{E}$	$\hat{\mathbf{n}}_C^{\mathcal{E}}$	$[1, 0, 0]^T$	–
Direction vector of laser beam in $\mathcal{E}$	$\hat{\mathbf{n}}_L^{\mathcal{E}}$	$[1, 0, 0]^T$	–
Surface normal of sensor in $\mathcal{Q}$	$\hat{\mathbf{n}}_S^{\mathcal{Q}}$	$[0.995, 0, 0.0998]^T$	–
Radius of sensor	$r_S$	0.05	m
Position of camera in $\mathcal{E}$	$\mathbf{r}_{C/E}^{\mathcal{E}}$	$[0, 0.01, 0]^T$	m
Position of laser emitter in $\mathcal{E}$	$\mathbf{r}_{L/E}^{\mathcal{E}}$	$[0, -0.01, 0]^T$	m
Position of sensor in $\mathcal{Q}$	$\mathbf{r}_{S/Q}^{\mathcal{Q}}$	$[0, 0, 0.1]^T$	m
ETS response time constant	$\tau$	0.1	s
Camera horizontal field of view	$\varphi$	56	°

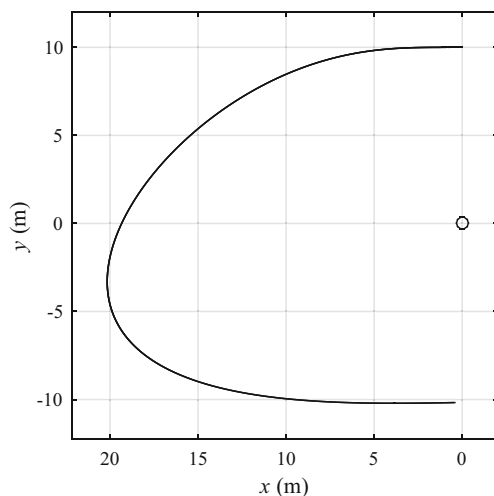
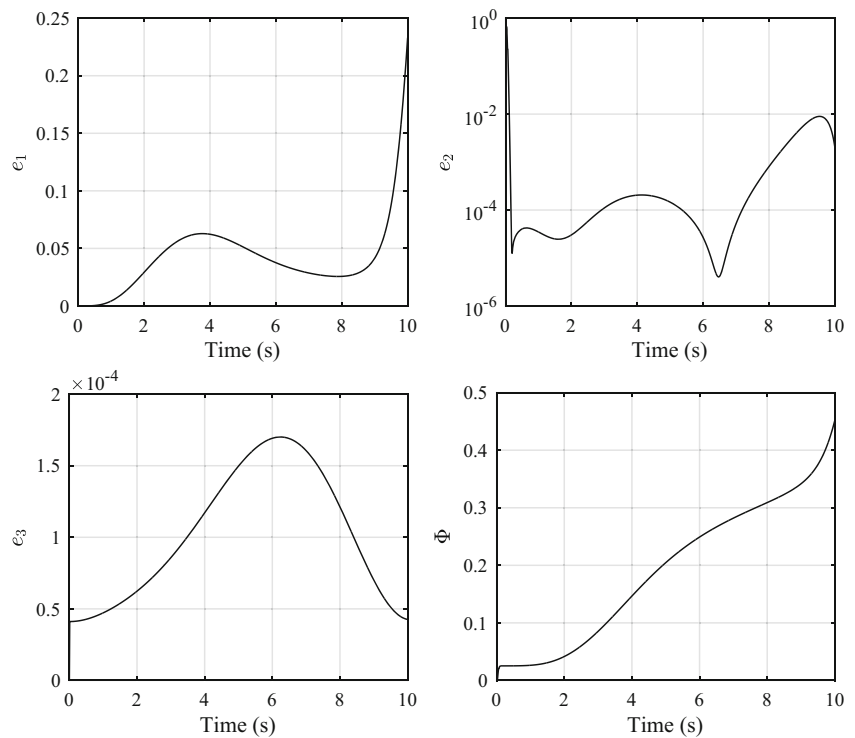


**Fig. 5** Near-optimal trajectory for a 10 s flight, determined by a two-parameter optimisation. Height remains constant at  $z(t) = -2$  m

for the two-parameter set  $\chi = \{\dot{x}_0, \dot{x}_f\}$  over the time range  $[t_0, t_f]$ , with initial values  $\chi_0 = \{5, -5\}$ .

Again employing the Nelder-Mead algorithm, a local minima is identified at the coordinates given in Table 3. The resulting trajectory is shown in Fig. 8. The trajectory has noticeably greater symmetry about the  $x$ -axis in this instance. This property is complemented by the similar initial and final velocity parameters after optimisation. The constituent error histories and cumulative cost function during this longer flight are provided in Fig. 9. It is clear that the most heavily-weighted errors—those relating to the beam angle of incidence,  $e_1$ , and spot error,  $e_2$ —are significantly reduced in comparison to the 10 second flight. Whilst the distance travelled by the quadrotor is greater than in the 10 s flight, the motion is comparatively less aggressive. This results in the ETS tracking the quadrotor with greater accuracy, resulting in a lower spot tracking error  $e_2$ . Additionally, the slower manoeuvre allows the quadrotor’s yaw controller to better track the ETS position,

**Fig. 6** Histories of optimisation errors and cost function for two-parameter optimisation of 10 s flight



reducing the angle of incidence error  $e_1$ . The greater range of the quadrotor results in a larger beam range error  $e_3$ . However, as this error is weighted very lightly, the cost function is lower ( $\Phi_{\min} = 0.1333$ ) at the end of the flight

than in Case 1 ( $\Phi_{\min} = 0.4546$ ). This is despite the flight time being twice that of the 10 s manoeuvre.

Once again, considering Eq. 27 as a non-linear function of two properties allows this function to be visualised as a two-dimensional contour map (Fig. 10). In this case, it is apparent that the global minima within the given bounds has not been found. Rather, a local minima closer to the initial search location has been identified. Again, it cannot be stated with certainty that the lower minima in this figure, at the approximate location (3, -5.1), is the global minima. However, it is clearly the more-optimal solution in the vicinity of the initial search location.

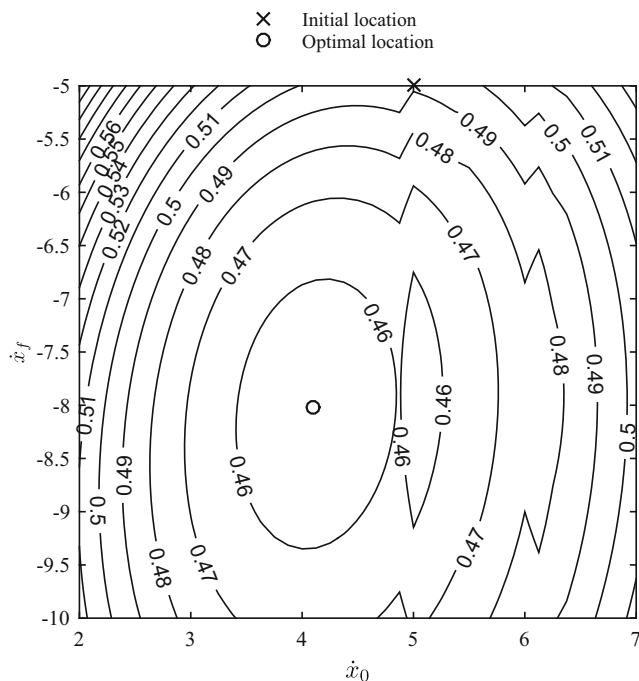


**Fig. 7** Cost function surface for two-parameter optimisation of 10 s flight

### 4.3 Optimisation with Four Variables

The trajectory is parameterised by four variables  $\chi = \{\dot{x}_0, \dot{z}_0, \dot{x}_f, \dot{z}_f\}$ , whilst the remainder of the parameter set  $\hat{\chi} \setminus \chi$  is constant. The optimisation is again performed for two test cases. As Fig. 10 demonstrates, the choice of initial search location can affect the minima identified by the

**Table 2** Trajectory parameters obtained from two-parameter optimisation of 10 s flight

Parameter	$\chi_0$	$\chi_{\min}$
$\dot{x}_0$	5.000	4.105
$\dot{x}_f$	-5.000	-8.023

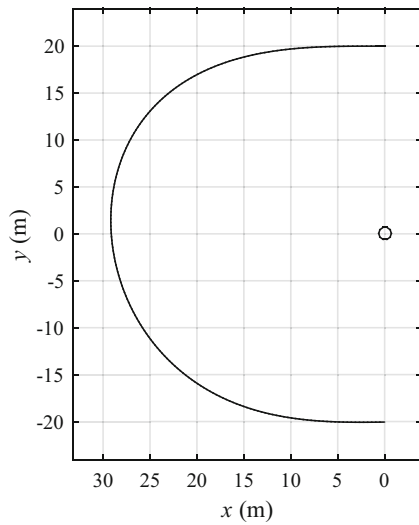


**Fig. 8** Near-optimal trajectory for a 20 s flight, determined by a two-parameter optimisation. Height remains constant at  $z(t) = -2$  m

Nelder-Mead algorithm. Therefore, each case in the four-variable test employs a unique set of initial parameters. For each case, the quadrotor trajectory is optimised for WPT for the four aforementioned variables only.

In each case, the non-linear function  $\Phi(\chi)$  is the same. It is simply the initial values of the parameter set  $\chi$  which is varied. As such, the quadrotor trajectory is specified by the fixed initial position  $\mathbf{r}_0 = [0, 10, -2]^T$  at  $t_0 = 0$  s and  $\mathbf{r}_f = [0, -10, -2]^T$  at  $t_f = 10$  s. The remaining

velocity parameters in  $\hat{\chi} \setminus \chi$  are fixed at  $\{\dot{y}_0, \dot{z}_0\} = 0$ . The trajectory is then optimised for the parameter set  $\chi = \{\dot{x}_0, \dot{z}_0, \dot{x}_f, \dot{z}_f\}$  over the range  $[t_0, t_f]$ . In each case, the Nelder-Mead algorithm is used to find a local minima in the vicinity of the initial search location.

### 4.3.1 Case 1: First Set of Initial Parameters

The first case considers the minimisation of the four-dimensional cost function  $\Phi(\chi)$  with the initial parameter set  $\chi = \{5, 0, -5, 0\}$ . The location of the identified local minimum is given in Table 5, whilst the value of this minimum is  $\Phi_{\min} = 0.3940$ .

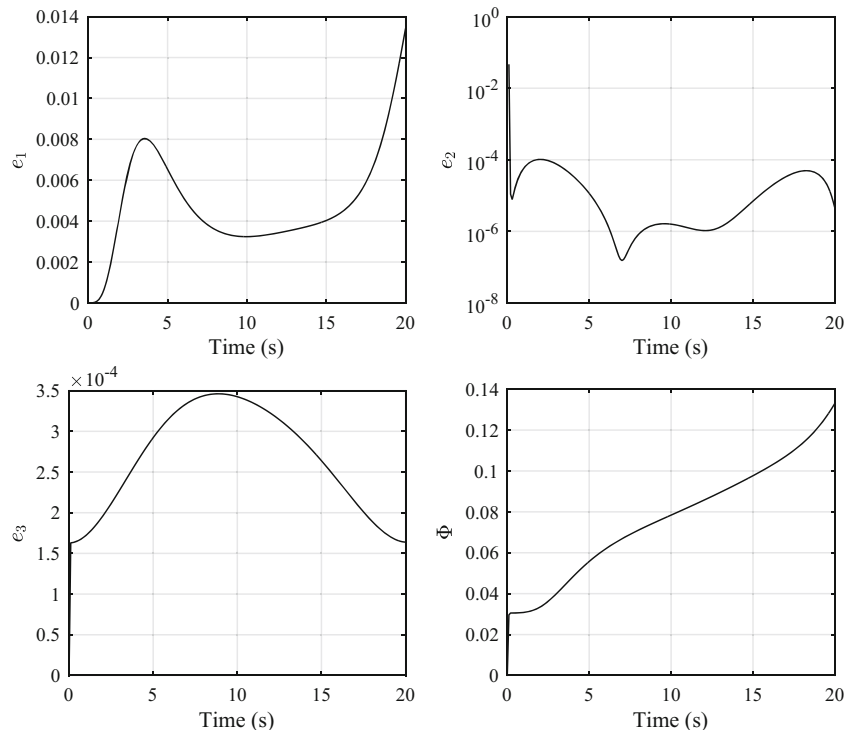
### 4.3.2 Case 2: Second Set of Initial Parameters

The second case considers the minimisation of the four-dimensional cost function  $\Phi(\chi)$  with the initial parameter set  $\chi = \{5, -1.5, -8, 1.5\}$ . The location of the identified local minimum is given in Table 5, whilst the value of this minimum is  $\Phi_{\min} = 0.3823$ .

### 4.3.3 Comparison of Results

The initial search location of Case 2 is deliberately chosen such that it is closer to the identified minimum of Case 1 than the initial search location of that case. Despite this choice of initial parameter set, the local minima of the Case optimisation is found at a different location.

**Fig. 9** Histories of optimisation errors and cost function for two parameter optimisation of 20 s flight



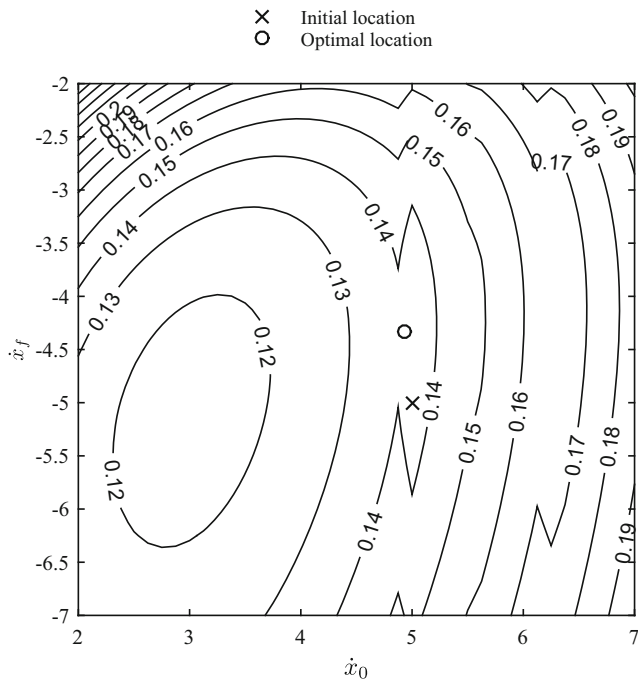


**Fig. 10** Cost function surface for two-variable optimisation of 20 s flight

The quadrotor’s trajectory for each optimised parameter set  $\chi$  is given in Fig. 11. It is readily apparent that the difference in optimised trajectory properties from Case 1 to Case 2 results in a slight but non-negligible change in the quadrotor’s trajectory.

The differences between the two cases may be further scrutinised by considering the constituent error and cost function histories, given in Fig. 12. Both cases demonstrate similar trends in both errors and cost function. Indeed, the minimised cost function for Case 1,  $\Phi_{\min} = 0.3940$  is remarkably similar to that of Case 2,  $\Phi_{\min} = 0.3823$ . Aside from a slight difference in the lightly-weighted beam range error  $e_3$ , the primary difference in each case manifests in the beam spot error  $e_2$ . Whilst the difference in  $e_2$  between the two cases varies throughout the manoeuvre, it is the large spike at the beginning which provides a residual in  $\Phi(t)$ , clearly present in the cost function history. A slight difference in  $e_2$  at the end of the manoeuvre then has the effect of reducing this gap, resulting in the very slight difference in  $\Phi_{\min}$ .

**Table 3** Trajectory parameters obtained from two-parameter optimisation of 20 s flight

Parameter	$\chi_0$	$\chi_{\min}$
$\dot{x}_0$	5.000	4.924
$\dot{x}_f$	-5.000	-4.338

**Table 4** Trajectory parameters obtained from four-parameter optimisation with first set of initial conditions

Parameter	$\chi_0$	$\chi_{\min}$
$\dot{x}_0$	5.000	5.142
$\dot{z}_0$	0.000	-1.701
$\dot{x}_f$	-5.000	-9.044
$\dot{z}_f$	0.000	2.337

It may thus be concluded that, for the four-parameter optimisation, a change in initial parameters has a negligible effect on the beam-steering and angle of incidence errors and the associated safety concerns.

The results of Case 1 may also be compared to Case 1 of the two-parameter optimisation. Both scenarios are near-identical, with the only difference being that  $\dot{z}_0$  and  $\dot{z}_f$  are fixed at zero in the two-parameter optimisation, whilst they are variable in the four-parameter optimisation, with only their initial values set to zero. Thus Case 1 of the four-dimensional cost function may be considered an extension of Case 1 of the two-dimensional cost function, with additional flexibility in the optimisation arising from the two additional variables. It is then expected that the four-dimensional problem will provide a minimum either equal to or lower than that provided by the two-dimensional problem. This is indeed found to be the case, with  $\Phi_{\min} = 0.4546$  for the two-parameter optimisation and  $\Phi_{\min} = 0.3940$  for the four-parameter case.

#### 4.4 Optimisation with Six Variables

The flexibility of the optimisation in selecting a trajectory may be further increased by the addition of further variables.

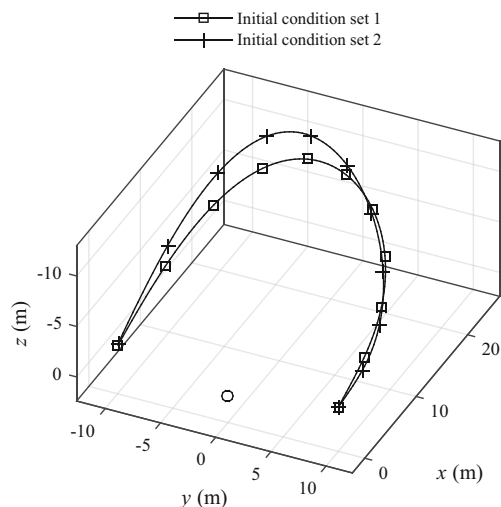
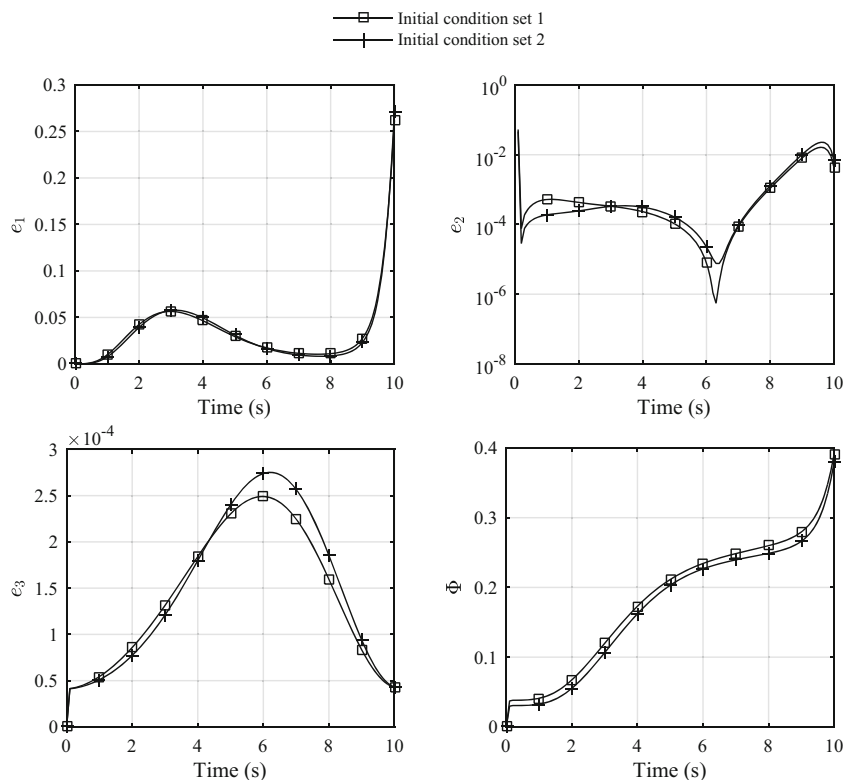


**Fig. 11** Near-optimal trajectory for a 10 s flight, determined by a four-parameter optimisation

**Fig. 12** Histories of optimisation errors and cost function for four parameter optimisation, with two sets of initial conditions



The trajectory is now parameterised by six variables  $\chi = \{\dot{x}_0, \dot{y}_0, \dot{z}_0, \dot{x}_f, \dot{y}_f, \dot{z}_f\}$ , allowing full optimisation of the velocity parameters. The remainder of the parameter set  $\hat{\chi} \setminus \chi$  is constant.

As highlighted by the four-parameter optimisation results, the choice of initial parameter set  $\chi_0$  can impact the identified minima. Whilst the error histories in the two cases considered by the four-parameter problem were very similar and the difference in  $\Phi_{\min}$  values negligible, it cannot be said with certainty that such similar solutions will always be found. A greater parameter size only increases the potential for a cost-function with multiple and varied minima.

A third comparison is thus considered. Given the same six-dimensional problem  $\Phi(\chi)$ , with identical trajectory constants and initial variables, two different approaches to finding its minimum may be presented. In the first, the

Nelder-Mead algorithm is used to identify the minimum, given some initial parameter set  $\chi_0 \in \mathbb{R}^6$ . In the second approach, the same initial parameters are employed, but the optimisation is performed using the simulated annealing (SA) algorithm. SA’s ability to “jump” out of local minima increases the probability of identifying a global minima, at least within the specified bounds. As SA provides only an approximate solution  $\chi_{SA}$  in the vicinity of a minimum, the Nelder-Mead algorithm is again used to refine the solution, using  $\chi_{SA}$  as the initial search location. Thus, the second approach essentially uses SA to narrow the search space around the global minima. This then allows the line-search algorithm to finish the optimisation.

In both cases, the quadrotor trajectory is specified by the fixed initial position  $\mathbf{r}_0 = [0, 10, -2]^T$  at  $t_0 = 0$  s and

**Table 5** Trajectory parameters obtained from four-parameter optimisation with second set of initial conditions

Parameter	$\chi_0$	$\chi_{\min}$
$\dot{x}_0$	5.000	4.861
$\dot{z}_0$	-1.500	-0.603
$\dot{x}_f$	-8.000	-9.483
$\dot{z}_f$	1.500	4.002

**Table 6** Trajectory parameters obtained from six-parameter optimisation with arbitrary initial conditions

Parameter	$\chi_0$	$\chi_{\min}$
$\dot{x}_0$	5.000	4.733
$\dot{y}_0$	0.000	1.892
$\dot{z}_0$	0.000	-2.757
$\dot{x}_f$	-5.000	-9.953
$\dot{y}_f$	0.000	-0.383
$\dot{z}_f$	0.000	1.116

**Table 7** Initial and boundary conditions and optimised parameter set from simulated annealing optimisation

Parameter	$\chi_{ub}$	$\chi_{lb}$	$\chi_0$	$\chi_{SA}$
$\dot{x}_0$	0	30	5	3.961
$\dot{y}_0$	-10	10	0	2.755
$\dot{z}_0$	-10	10	0	-0.869
$\dot{x}_f$	-30	0	-5	-13.114
$\dot{y}_f$	-10	10	0	0.152
$\dot{z}_f$	-10	10	0	5.040

fixed final position  $\mathbf{r}_f = [0, -10, -2]^T$  at  $t_f = 10$  s. The trajectory is then optimised for the parameter set  $\chi \in \mathbb{R}^6$  over the range  $[t_0, t_f]$ .

**4.4.1 Case 1: Arbitrary Initial Parameters**

In the first case, the initial parameter set is chosen arbitrarily to be  $\chi_0 = \{5, 0, 0, -5, 0, 0\}$ . This is used as the initial search location by the Nelder-Mead algorithm. The resulting minimum is found at the coordinates given in Table 6, with the value  $\Phi_{min} = 0.3846$ .

**4.4.2 Case 2: Narrowed Initial Parameters**

In the second case, the same initial parameter set  $\chi_0 = \{5, 0, 0, -5, 0, 0\}$  is employed. Simulated annealing is then used to narrow the search space around the global minimum within some bounds. The upper and lower bounds,  $\chi_{ub}$  and  $\chi_{lb}$  respectively, are given in Table 7. The bounds are

chosen such that they provide a large search space around the identified minimum of Case 1.

The SA optimisation provides an approximate location for the bounded global minimum, given in Table 7 as  $\chi_{SA}$ . The cost function has value  $\Phi_{min} = 0.3806$  at these coordinates. This is then used as the initial search location for the simpler Nelder-Mead algorithm. Table 8 shows the SA-provided initial co-ordinates for the line-search optimisation and optimised parameters resulting from this algorithm. The value of the minimum is found to be  $\Phi_{min} = 0.3545$ .

**4.4.3 Comparison of Results**

As expected, the minimum identified from the narrowed initial parameter,  $\Phi_{min} = 0.3545$ , is lower than that identified from the arbitrary initial parameter set,  $\Phi_{min} = 0.3846$ . The simulated annealing algorithm thus succeeds in improving the results of the line-search algorithm. This is at the cost of time, with simulated annealing requiring at least four times the number of function calls required by the Nelder-Mead algorithm.

The optimised trajectories resulting from each case are compared in Fig. 13. Additionally, the trajectory resulting from the narrowed parameter set of the SA algorithm is presented. It is clear that, whilst the SA and Case 1 line-search algorithms both employ the same initial parameters, they result in significantly different trajectories. The trajectory found by the Case 2 line-search is then a refinement of the SA optimisation. As such, it is shown to be similar to the SA-optimised trajectory.

The constituent error and cost function histories may again be compared for the two cases. The beam spot error  $e_2$  again demonstrates the largest difference. The beam length error  $e_3$  also displays a non-negligible difference, however this on an order of magnitude which has little impact on the cost function. It is apparent from the cost function history that the main contribution to the differing trajectories is from the beam spot error.

The combination of SA and Nelder-Mead algorithms has thus identified a trajectory which ensures superior beam-steering than that from using Nelder-Mead alone. The impact on the angle of incidence error, which primarily relates to the ability of the quadrotor to maintain line-of-sight with the ETS, is negligible.

The results of Case 1 may be compared to Case 1 in the more-restricted two- and four-parameter optimisations. Again, each scenario is near-identical, with only the number of variables changed. The constants of the two-parameter optimisation define the initial values for the variables in the four- and six-parameter optimisations. It is again expected that the six-dimensional problem yield a lower cost function after optimisation, due to the greater flexibility arising from a large parameter set. This is indeed the case, with  $\Phi_{min} =$

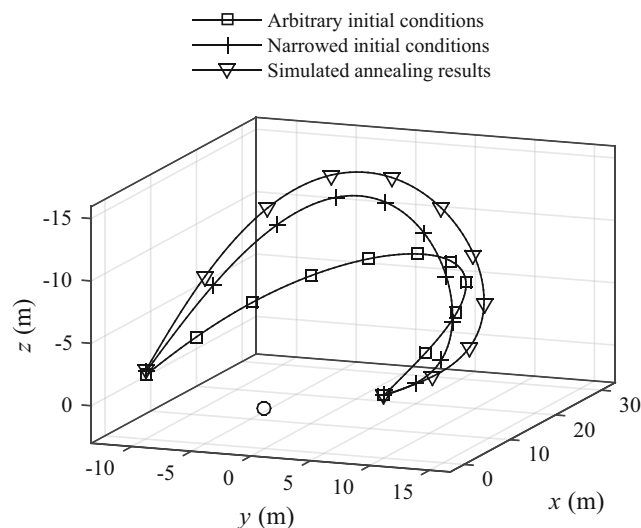
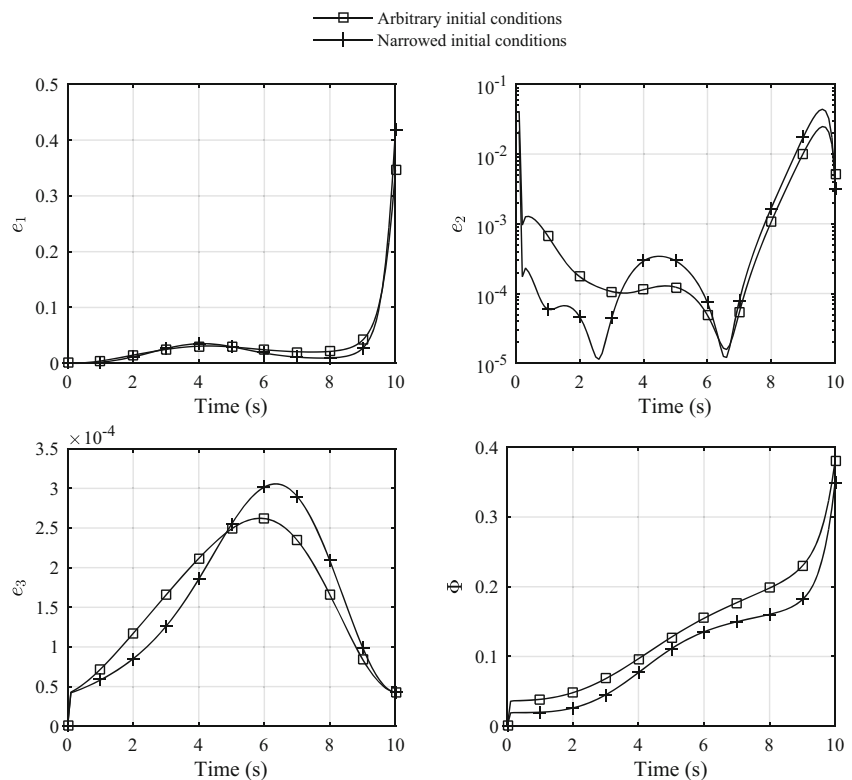


**Fig. 13** Near-optimal trajectory for a 10 s flight, determined by a six-parameter optimisation

**Fig. 14** Histories of optimisation errors and cost function for six parameter optimisation, with two sets of initial conditions



0.3545 being lower than the minimum for the two-parameter ( $\Phi_{\min} = 0.4546$ ) or four-parameter ( $\Phi_{\min} = 0.3940$ ) optimisations.

### 4.5 Computational Load

As indicated in the previous sections, an increase in the number of variables employed in the optimisation algorithm results in a decrease in the minimised cost function value  $\Phi_{\min}$ . It is clear from Table 9 that increasing the number of variables from two to six, with otherwise identical initial conditions, results in a reduction in the identified minimum of 15.4%. This value may be further reduced by first employing simulated annealing to obtain an estimate of the minimum location and then refining this result with the Nelder-Mead algorithm, resulting in a decrease of 22% from the two-variable optimisation to the six.

**Table 8** Trajectory parameters obtained from six-parameter optimisation with narrowed initial conditions

Parameter	$\chi_0$	$\chi_{\min}$
$\dot{x}_0$	3.961	3.681
$\dot{y}_0$	2.755	1.403
$\dot{z}_0$	-0.869	-0.292
$\dot{x}_f$	-13.114	-10.706
$\dot{y}_f$	0.152	-1.379
$\dot{z}_f$	5.040	4.908

However, this decrease in minimum, and consequent improvement in operational safety and efficiency, comes at the cost of computational efficiency. Consider Table 9. With an average runtime per call of 3.56 s for the optimisation function described by Eqs. 27 and 28, the two-variable optimisation makes 74 calls in 4.4 min for Case 1. In contrast, the four-variable optimisation makes 879 calls in 52.2 min for Case 1, whilst the six-variable optimisation makes 953 calls in 55.92 min, again for Case 1. This corresponds to an increase in execution time of 1,187% for a 15.4% reduction in cost function output, for the increase from two to six variables. Employing simulated annealing to further minimise the cost function results in an execution time increase of 6,463% for a 22% reduction.

**Table 9** Computational expenditure and cost function result for each experiment

Variables	Case	$\Phi_{\min}$	Runtime (s)	Calls
2	1	0.4546	263.41	74
4	1	0.3940	3,131.45	879
4	2	0.3823	1,543.97	432
6	1	0.3846	3,355.08	953
6	2 (SA)	0.3806	15,511.20	4,244
6	2 (NM)	0.3545	2,158.16	613
6	2 (net)	0.3545	17,669.36	4,857

Case 2 is omitted for the two-variable optimisation, as it considers a longer trajectory

Ultimately, a relatively small reduction in cost function value may not be worth the considerable increase in computational expenditure. An execution time of almost 5 hours, as is the case with the combined six-variable simulated annealing/Nelder-Mead optimisation, is impractical for even offline optimisation. Conversely, an execution time of 4.4 min may be accommodated in-flight by performing the optimisation in advance of the manoeuvre. Note that these experiments were performed in MATLAB on a computer with a 3rd-generation i7 processor and 16 GB of RAM. Further reductions in runtime may be made by employing more powerful hardware and a compiled programming language.

## 5 Extension to More Complex Scenarios

The scenario presented in this paper considers a single quadrotor receiving power from a single energy transmission system. Logical extensions of this scenario include increased quantities of both quadrotor and ETS.

Consider first an increase in ETS numbers. This could simply result in multiple instances of the scenario described in Section 2. Thus, a single ETS would power a single quadrotor, but at multiple instances in different locations. Alternatively, a single quadrotor could be powered by multiple ETSs. This would impact the optimisation cost function, which would have to consider the geometry of all active ETSs with respect to the single quadrotor. The benefit of employing multiple laser emitters is clearly the increase in power received by the quadrotor. The downside to this is the increased risk in one or more of the laser beams missing or overfilling the receiving sensor. Optimising the quadrotor trajectory for multiple incoming laser vectors may result in suboptimal solutions for all vectors. Thus, whilst received power may increase with respect to a single ETS transmission, the safety may decrease to unacceptable levels.

This approach may be refined by providing feedback on the quadrotor position and attitude to the ETS controllers. This would allow the ETS to deactivate when the errors described in Section 3.2 exceed a specified tolerance. The trajectory may then be defined such that it enables a sequence of power transmissions from successive ETSs, perhaps with some overlap. Additionally, there is no restriction that each ETS must feature identical capabilities. Variety in the laser power and beam width could facilitate more flexible scenarios. An example would be a persistent low-power beam, with minimal risk to the surrounding environment in the event of missing its target, supplemented by a sequence of shorter-duration, high-power transmissions. In this case, the cost function would consider only the laser vectors which are active or expected to be active soon.

An increase in the number of the quadrotors is important to consider, due to the potential of collaborative missions such as construction or coordinated search and reconnaissance. The simplest scenario in a multi-vehicle operation would involve sequential charging of quadrotors by either a single or multiple laser emitters. In the former case, the optimisation would be performed much as it has been in this paper, considering the relative geometry of the quadrotor and single laser vector. In the latter case, the optimisation may proceed as described above. A benefit of having multiple quadrotors charging in succession, or even a single quadrotor charging repeatedly, is the ability to provide in-flight refinement of the process. This could involve online parameter estimation and system identification of the multi-agent system. Evaluation of expected geometric errors against measured values in real-time could be used to update the system models and ensure that the trajectory optimisation becomes more accurate with each successive transmission.

## 6 Conclusions

This paper demonstrates one possible solution to the issue of safety in wireless power transmission. It is required that the high-powered laser emitted by an energy transmission system remains incident on the intended target and nothing else. This is ensured by optimising the trajectory of the quadrotor, carrying the target sensor, such that the beam is always on-target and at a near-normal angle of incidence.

A number of cases were presented, from which some conclusions may be drawn. First, it is clear that increasing the parameter set  $\chi$  for the optimisation results in superior optimisation results and lower risk in the beam transmission. Second, a relatively conservative change in initial parameters can result in a noticeable change in trajectory, but minimal impact on the optimisation errors (Fig. 12). Use of a global optimisation algorithm such as simulated annealing to approximate the location of a global (within some bounds) minimum can produce far more favourable results. The impact on the optimisation errors is shown to be non-trivial, although not significant (Fig. 14). Conversely, the impact on the trajectory is shown to be significant (Fig. 13).

## 7 Future Work

The constituent error histories of the optimised flights indicate two areas for further investigation. First, the beam spot error  $e_2$  is demonstrably large at the beginning of the manoeuvre in each case. As the ETS's target-tracking and beam-steering controller passes through its transient phase,

this error becomes negligible. Second, for the remainder of the manoeuvre, the greatest error occurs in the angle of incidence of the beam with the photovoltaic sensor, minimised through  $e_1$ . This error is related to two properties. First, the angle of incidence in the horizontal plane is determined primarily by the yaw angle of the quadrotor. Thus, given a fixed closed-loop yaw response, the optimised trajectory must be sufficient slow as to allow the quadrotor to maintain line-of-sight tracking of the ETS. Second, the component of angle of incidence in the vertical plane is determined primarily by the quadrotor roll and pitch angles. These are not manually specified, but determined by the vehicle's acceleration along the trajectory. Therefore, the position trajectory must be defined such that the roll and pitch responses during the manoeuvre minimise the angle of incidence in the vertical plane. Investigation into further minimising these specific errors is therefore pertinent.

As highlighted by the optimisation results, increasing the number of variables results in greater flexibility in the optimised trajectory. In addition to employing the full parameter set  $\hat{\chi}$ , it is also possible to introduce other system properties as variables. These could include the trajectory time  $t_f$  and properties of the quadrotor controller. Additionally, adjustment of other parameters, such as the search space boundaries required by simulated annealing, can impact the results of the optimisation by identifying lower minima at large distances from the initial search location.

Extension of the trajectory optimisation to scenarios with greater numbers of quadrotors and/or ETSs has been discussed. Investigation of these scenarios would not only require optimisation of the trajectory whilst charging, but also consideration of other factors. Key issues include relative positions of ETSs, diversity in ETS capabilities, sequencing and timing of quadrotor charging operations and optimal numbers of ETSs and quadrotors.

Finally, more realistic scenarios may be considered. For simplicity, very short manoeuvres were considered in this paper. In future efforts, it would be pertinent to investigate trajectories of longer duration and at greater ranges from the energy transfer system. At such ranges, risk alleviation is even more crucial due to the larger beam diameter and effects of jitter in the beam-steering.

**Open Access** This article is distributed under the terms of the Creative Commons Attribution 4.0 International License (<http://creativecommons.org/licenses/by/4.0/>), which permits unrestricted use, distribution, and reproduction in any medium, provided you give appropriate credit to the original author(s) and the source, provide a link to the Creative Commons license, and indicate if changes were made.

**Publisher's Note** Springer Nature remains neutral with regard to jurisdictional claims in published maps and institutional affiliations.

## References

- Achtelik, M.C., Stumpf, J., Gurdan, D., Doth, K.M.: Design of a flexible high performance quadcopter platform breaking the MAV endurance record with laser power beaming. In: 2011 IEEE/RSJ International Conference on Intelligent Robots and Systems (IROS), pp. 5166–5172. IEEE, San Francisco (2011)
- Anderson, D.: Sightline jitter minimisation and shaping using nonlinear friction compensation. *Int. J. Optoelectron.* **1**, 259–283 (2007)
- Anderson, D.: Evolutionary algorithms in airborne surveillance systems: image enhancement via optimal sightline control. *Proc. IMechE Part G: J. Aerosp. Eng.* **225**, 1097–1108 (2011)
- Anderson, D., McGookin, M., Brignall, N.: Fast model predictive control of the nadir singularity in electro-optic systems. *J. Guid. Control. Dyn.* **32**(2), 626–632 (2009)
- Bagiev, M., Thomson, D., Anderson, D., Murray-Smith, D.: Predictive inverse simulation of helicopters in aggressive manoeuvring flight. *Aeronaut. J.* **116**(1175), 87–98 (2012)
- Bouabdallah, S., Murrieri, P., Siegwart, R.: Design and control of an indoor micro quadrotor. In: Proceedings of IEEE International Conference on Robotics and Automation, pp. 4393–4398. IEEE (2004). <https://doi.org/10.1109/ROBOT.2004.1302409>
- Brown, W.C.: Experiments involving a microwave beam to power and position a helicopter. *IEEE Trans. Aerosp. Electron. Syst.* **AES-5**(5), 692–702 (1969)
- Brown, W.: The history of wireless power transmission. *Solar Energy* **56**(1), 3–21 (1996)
- Černý, V.: Thermodynamical approach to the traveling salesman problem: an efficient simulation algorithm. *J. Optim. Theory Appl.* **45**(1), 41–51 (1985)
- Cowling, I.D., Yakimenko, O.A., Whidborne, J.F., Cooke, A.K.: A prototype of an autonomous controller for a quadrotor UAV. In: European Control Conference, pp. 1–8 (2007)
- Dickinson, R.M., Grey, J.: Lasers for wireless power transmission. Tech. rep., Jet Propulsion Laboratory (1999)
- Ireland, M., Anderson, D.: Development of navigation algorithms for nap-of-the-earth uav flight in a constrained urban environment. In: Proceedings of the 28th International Congress of the Aeronautical Sciences. Brisbane (2012)
- Ireland, M., Vargas, A., Anderson, D.: A comparison of closed-loop performance of multirotor configurations using non-linear dynamic inversion control. *Aerospace* **2**(2), 325–352 (2015). <https://doi.org/10.3390/aerospace2020325>
- Kirkpatrick, S., Gelatt, C., Vecchi, M.: Optimization by simulated annealing. *Science* **220**(4598), 671–680 (1983)
- Lagarias, J.C., Reeds, J.A., Wright, M.H., Wright, P.E.: Convergence properties of the Nelder-Mead simplex method in low dimensions. *SIAM Journal on Optimization* **9**(1), 112–147 (1998). <https://doi.org/10.1137/S1052623496303470>
- Metropolis, N., Rosenbluth, A.W., Rosenbluth, M.N., Teller, A.H., Teller, E.: Equation of state calculations by fast computing machines. *J. Chem. Phys.* **21**, 1087–1092 (1953). <https://doi.org/10.1063/1.1699114>
- Nelder, J.A., Mead, R.: A simplex method for function minimization. *Comput. J.* **7**, 308–313 (1965)
- Nugent, T., Kare, J.: Laser Power for UAVs. White paper (2010)
- Nugent, T., Kare, J., Bashford, D., Erickson, C., Alexander, J.: 12-hour hover: flight demonstration of a laser-powered quadcopter. Tech. rep., LaserMotive (2011)
- Nugent, T.J., Kare, J.T.: Laser power beaming for defense and security applications. Tech. rep., LaserMotive (2011)
- Voos, H.: Nonlinear control of a quadrotor micro-UAV using feedback-linearization. In: Proceedings of the 2009 IEEE International Conference on Mechatronics. IEEE, Malaga (2009). <https://doi.org/10.1109/ICMECH.2009.4957154>

**Murray L. Ireland** received his PhD in non-linear control and trajectory optimisation for UAVs from the University of Glasgow in 2014. His research interests include non-linear dynamics, inverse simulation, machine learning and space systems.

**David Anderson** is a Senior Lecturer in Aerospace Systems at the University of Glasgow. He is currently developing a bespoke multi-agent, multi-resolution framework for autonomous systems research. His other interests include rotorcraft simulation, sightline control and platform survivability.